Inorganic Chemistry

ARTICLE

pubs.acs.org/IC

$Sm_{2-x}Dy_xZr_2O_7$ Pyrochlores: Probing Order−Disorder Dynamics and Multifunctionality

Farheen N. Sayed,[†] V. Grover,*[,†] K. Bhattacharyya,[†] D. Jain,[†] A. Arya,[‡] C. G. S. Pillai, and A. K. Tyagi*[,†]

[†]Chemistry Division and [‡]Materials Science Division, Bhabha Atomic Research Centre, Mumbai 400085, India

ABSTRACT: The present work involves the synthesis of a series of $Sm_{2-x}Dy_xZr_2O_7$ compounds ($0.0 \le x \le 2.0$) by a controlled gel combustion process. The powders were thoroughly analyzed by powder X-ray diffraction (XRD), Raman spectroscopy, scanning electron microscopy, and diffuse-reflectance UV−visible spectroscopy. The powder XRD studies revealed the system to be single-phasic throughout with retention of pyrochlore-type ordering until 40 mol % of Dy^{3+}, beyond which the pyrochlore lattice gives way to the defect fluorite structure. Interestingly, Raman spectroscopic studies (as against XRD studies) showed retention of pyrochlore-type ordering throughout the homogeneity range of the compositions studied. This is perhaps the first study that reports retention of a weak pyrochlore-type superstructure in the $Dy_2Zr_2O_7$ system, which was otherwise known to crystallize in the defect fluorite system. The ionic conductivity measurements showed an increase in the activation energy (E_a) with an increase in the mole percent of Dy^{3+} owing to the decreased mobility with an increase in the degree of disorder. The system possesses a tunable band gap with varying amounts of Dy^{3+}. First-principles calculations were performed to support a decrease in the band gap of the doped system with an increase in the Dy^{3+} content. The potential as photocatalysts of some of these compositions was explored, and they exhibited high photocatalytic activity for degradation of xylenol orange, with $t_{1/2}$ increasing from pure $Sm_2Zr_2O_7$ to pure $Dy_2Zr_2O_7$.

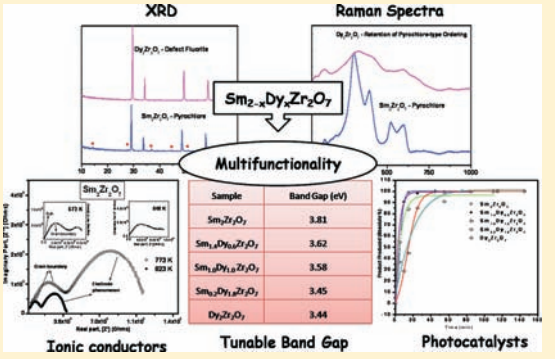

1. INTRODUCTION

The pyrochlore structure $A_2B_2O_7$ with space group $Fd3m$ and $Z = 8$ ($A_4B_4O_{12}O'_2$ for the primitive cell) can be described as a fluorite superstructure, wherein BO_6 octahedra are linked through corners forming a $[B_4O_{12}]_{infinite}$ framework in which is imbricated a $[A_4O'_2]_{infinite}$ network of A_4O tetrahedra with an anti *p*-cristobalite structure.[1,2] Elemental versatility ensures that materials with $A_2B_2O_7$ composition (where A, in general, represents rare-earth elements or their mixtures in a 3+ oxidation state and B denotes a fourth group transition-metal element or their mixtures in a 4+ oxidation state)[3,4] have broad application potential such as in fast-ion (mainly anion) conductivity and geometrically frustrated magnetism[5−13] and as light emitters, display devices, optical telecommunication components, lasers, and biolabels.[7,14−18] They are viable nuclear waste host materials because of their structural compatibility with radionuclide species.[5,19]

The intriguing crystal chemistry originating from the cation and anion stoichiometry and compositions has also generated interest for extensive crystallographic studies in pyrochlore-type materials. The pyrochlore lattice is a cation-ordered anion-deficient fluorite lattice. For the completely ordered pyrochlore $A_2B_2O_7$, the phase stability of the superstructure is primarily determined by the A and B site cation radius ratio. It has been reported in the literature that the pyrochlore lattice is supported by a radius ratio, r_A/r_B, lying between 1.46 and 1.78. The order−disorder transition in the pyrochlores can be brought about by substitution as well as by heating to higher temperatures.[20] It has been suggested by various groups that A- and B-site substitution has tremendous bearing on the energetics of defect formation and the order−disorder transitions.[21−24]. Glerup et al.[25] have reported Rietveld analysis and Raman scattering on the series $Y_2Ti_{2-y}Zr_yO_7$ and concluded that, with an increase in the Zr content, the system undergoes a structural change from a perfect pyrochlore structure to a defect fluorite structure through an intermediate defect pyrochlore phase (partially disordered system). In view of all this, pyrochlores constitute an interesting class in the study of the phenomenon of order−disorder phase transition (pyrochlore ⇔ defect fluorite) and correlate them with their ionic conductivity.

The pyrochlore-structured oxides are known to be good ionic conductors, with some of them showing conductivity values comparable with yttria-stabilized zirconia (YSZ).[26] The YSZ-type materials are prone to dopant-vacancy association, leading to reduction in the ionic conductivity upon prolonged aging. Pyrochlores are endowed with intrinsic vacancies (which make them good ionic conductors) without the possibility of undergoing dopant-vacancy association. In the pyrochlore structure, the A^{3+} ions occupy the eight-coordinated 16d sites ($^1/_2$, $^1/_2$, $^1/_2$), the B^{4+} ions are at six-coordinated 16c sites (0, 0, 0), and the O^{2-} ions occupy the 48f sites (x, $^1/_8$, $^1/_8$) and 8b sites ($^3/_8$, $^3/_8$, $^3/_8$). The anion vacancy lies at 8a. It has been previously proposed by atomistic simulations that the most stable intrinsic

Received: October 21, 2010
Published: February 24, 2011

defect in these compounds is an oxygen Frenkel pair consisting of a vacant 48f position and an interstitial ion located at the 8b site[22,27] and that oxygen ion diffusion takes place by jumps from 48f to 48f sites in these materials. Thus, the oxygen conductivity in these disordered pyrochlores and/or fluorites depends essentially on the energy of formation of this kind of defect and on the ease of mobility of ions. There have been a few studies to correlate the ionic conductivity with the disorder prevailing in the structure.[28] The ionic conductivity also strongly depends on the preparation routes of the ceramics.[29] Soft chemical routes, such as gel combustion, can yield soft-agglomerated nanopowders with superior powder properties, which can ultimately give high-density pellets and, in turn, better ionic conductivity.

Adding another dimension in this already versatile class of materials is the fact that they can also be used as efficient photocatalysts by virtue of their ability to manipulate the electron/hole mobility by the choice of different combinations of elements at A and B sites and also by alteration of the occupancy of the oxygen sites. Among several others, it has been reported that Bi_2RNbO_7 (R = Y^{3+}, rare earth) materials are photoactive.[30,31] Efficient photocatalysis has also been observed for Sn^{2+}-incorporated pyrochlores by Uma et al.[32] They have also studied degradation of organic compounds by $AgSbO_3$ under UV−visible irradiation.[33] There are a few reports on the photocatalytic activity of the $RE_2Zr_2O_7$ series as well.[34] Hence, it would be of interest to explore the applicability of the present pyrochlore system in the photocatalytic decomposition of organic pollutants.

In this manuscript, an attempt has been made to vary the r_A/r_B ratio by varying the A-site cation in $Sm_2Zr_2O_7$, by substituting Dy^{3+}, and to investigate the accompanying structural changes. $Sm_2Zr_2O_7$ is a perfectly ordered pyrochlore, whereas $Dy_2Zr_2O_7$ is reported to be a defect fluorite. It would be of interest to observe the changes occurring in the intermediate compositions as Sm^{3+} is gradually replaced by Dy^{3+}. X-ray diffraction (XRD) analysis in conjunction with Raman spectroscopic studies was done on $Sm_{2-x}Dy_xZr_2O_7$ solid solutions to gain insight into the structural changes occurring in the system. To the best of our knowledge, no spectroscopic studies are available on the Dy^{3+}-substituted $Sm_2Zr_2O_7$ system in the literature. Electrical studies were performed on the $Sm_{2-x}Dy_xZr_2O_7$ system to correlate the trend in the ionic conductivity with the disorder induced in the system with Dy^{3+} substitution. Diffuse-reflectance ultraviolet−visible (DR-UV) studies were used to determine the band gap, and the given pyrochlore systems were further tested for their application as photocatalysts.

2. EXPERIMENTAL SECTION

Analytical reagent (AR) grade powders of Sm_2O_3, Dy_2O_3, $ZrO(NO_3)_2·H_2O$, and glycine were used as the starting reagents. Sm_2O_3 and Dy_2O_3 were preheated at 800 °C to remove adsorbed moisture and other gases. The rare-earth oxides were dissolved in a minimum amount of dilute HNO_3. The net oxidizing valencies of samarium nitrate, dysprosium nitrate, and zirconium oxynitrate and the reducing valencies of the fuel (glycine) were calculated using the valencies of the individual elements. On the basis of the stoichiometry concept,[35] the ratio of the oxidizing and reducing valencies should be unity. For this particular system, this implies that the ratio of the amounts of metal nitrates and/or oxynitrates to glycine should be 1:4.5. To synthesize different compositions in $Sm_{2-x}Dy_xZr_2O_7$ ($0.0 \le x \le 2.0$), the required amounts of reactants were weighed and dissolved and the appropriate amounts of glycine were added as fuel. Highly viscous liquids, termed "precursors", resulted after thermal dehydration of these solutions around 80 °C. As soon as the viscous liquid was formed, the temperature of the hot plate was raised to 250 °C. The precursors swelled and autoignited, with rapid evolution of a large volume of gases to produce voluminous powders. The as-synthesized powders were calcined at 700 °C in static air for 30 min to get rid of the decomposition products and excess carbon.

The products were characterized by powder XRD using monochromatized Cu Kα radiation on a Philips X-ray diffractometer (model PW 1927). Silicon was used as an external standard for correction due to instrumental broadening. The XRD patterns revealed the products to be in the nanosize regime, wherein the superstructure peaks of the pyrochlore phase were not visible. These powders were further compacted as pellets and sintered at 1450 °C in static air for 8 h to get the final sintered products.

The *POWDERX*[36] program was used to calculate the cell parameters of the obtained products.

The microstructure of the sintered pellets (1450 °C/8 h) was investigated using a AIS 210 scanning electron microscope (Mirero Inc., Seongnam-si, South Korea). The sintered pellets were coated with gold before the microstructural studies.

Raman spectroscopic measurements were carried out on a micro/macro-Raman spectrometer (LABRAM-1, France) using the 488-nm line of an Ar^+ ion laser for excitation. The scattered Raman signal was collected using a single-monochromator spectrometer equipped with a Peltier-cooled CCD detector in the backscattering geometry. Samples were used in the form of pellets, and the laser line was focused on a flat surface of the sample using an optical microscope (Olympus BX-40, 50× objective lens) connected to the spectrometer. The spectra recorded were averaged out of 50 scans with a time interval of 2 s and a resolution of 2 cm^{-1}.

Alternating-current (ac) impedance measurements were performed on the samples sintered at 1450 °C on an impedance analyzer [Solartron Impedance Gain phase analyzer (model SI 1260), Solartron Analytical, Hampshire, U.K.] in the frequency range from 10^6 Hz to 1 mHz. An ac voltage amplitude of 200 mV with a zero direct-current (dc) bias was applied across the two flat ends of the pellet-shaped samples (7.5−8 mm diameter; 0.9−1.0 mm thickness) during each measurement. Measurements were carried out in the temperature range of 250−800 °C in a static air atmosphere. Both flat surfaces of the samples were coated with conducting platinum paste and annealed at 1073 K (in order to have better contact with the platinum foil electrodes) before placing them into the indigenously designed and fabricated impedance cell. Tight contacts of the electrodes with the samples were ensured through a spring push mechanism of the cell during the entire experiment at each temperature. Both *Zplot 2.9b* (seriel no. ZPlot:7471-2) and *ZView 2.9b* (seriel no. ZPlot: 7471-2) [by Scribner Associates Inc., associated with the Solartron analyzer] were used to collect and analyze the impedance spectra of all of the samples, respectively.

DR-UV spectra were recorded in the 200−800 nm region, employing a Jasco model V-670 spectrometer. $BaSO_4$ was used as a reference.

These pyrochlore powders were evaluated as catalysts for degradation of xylenol orange dye in the presence of UV light. A 100 mL batch cylindrical pyrex glass reactor was employed. The irradiation source was a 400 W medium-pressure mercury lamp (SAIC) located inside a quartz tube, situated perpendicularly in the reactor with 170 mW cm^{-2} flux. For each set of experiments, the reaction mixture consisted of 50 mg of a catalyst powder suspended in 50 mL of an aqueous xylenol orange (10^{-5} M) solution. The suspensions were magnetically stirred for 30 min in the dark to establish an adsorption/desorption equilibrium. The dye−catalyst suspensions were irradiated under UV light, small aliquots were withdrawn at regular intervals of time (keeping the volume of the reaction mixture almost constant), and UV−visible spectra were recorded. A blank solution consisting of only an aqueous xylenol orange solution, without the catalyst, was also subjected to the same procedure to cancel

dx.doi.org/10.1021/ic200108u |*Inorg. Chem.* 2011, 50, 2354–2365

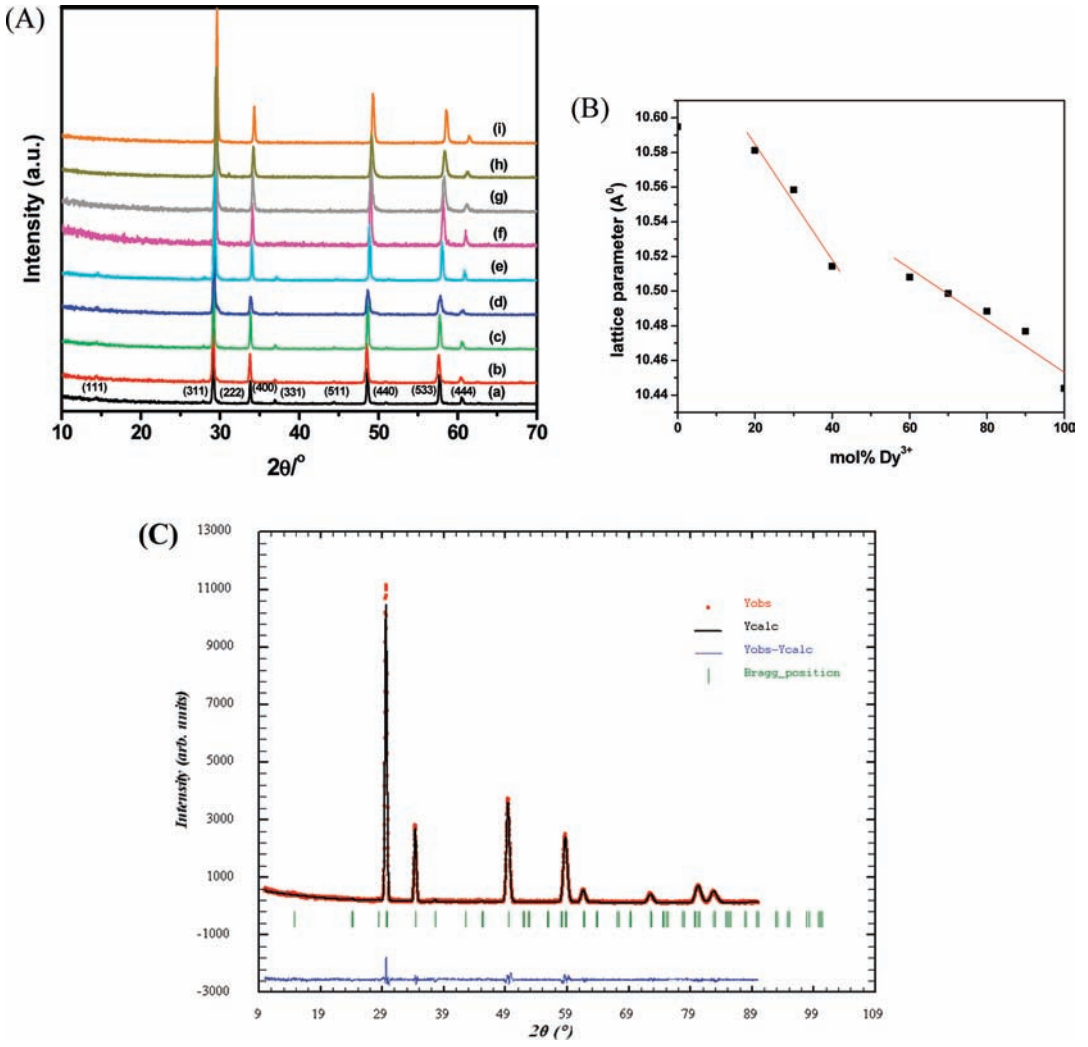

Figure 1. (A) XRD patterns of $Sm_{1-x}Dy_xZr_2O_7$, where x is (a) 0.0, (b) 0.20, (c) 0.40, (d) 0.60, (e) 0.80, (f) 1.2, (g) 1.6, (h) 1.8, and (i) 2.0. (B) Variation of the lattice parameter with the Dy^{3+} content. (C) Experimental (circles) and calculated (continuous lines) powder XRD patterns for $Sm_{1.4}Dy_{0.6}O_7$. The difference plot is given at the bottom. Bragg positions are indicated by the vertical markers below the observed pattern.

the effect of self-degradation of xylenol orange. The extent of reaction was monitored by measuring the decrease in the absorbance value at 435 and 570 nm using a Jasco V-670 UV−visible−NIR spectrometer. The amount of degraded dye was estimated using the formula $(A_0 - A_i)/A_0$, where A_i is the absorbance of a xylenol orange solution measured at different time intervals during the photodegradation process and A_0 is the absorbance of the initial xylenol orange solution after adsorption on the catalyst. The studies were carried out at neutral pH and ambient conditions.

3. RESULTS AND DISCUSSION

3.1. Structural and Electrical Characterization. *Results.* The XRD patterns of all of the products in $Sm_{2-x}Dy_xZr_2O_7$ ($0.0 \leq x \leq 2.0$) were recorded and carefully analyzed. The powder XRD patterns of various nominal compositions calcined at 700 °C consisted of main peaks belonging to the pyrochlore family. However, owing to the broad peaks and appreciable noise-to-signal ratio for powders calcined at 700 °C, the superstructure peaks were not visible. Heating the powders at 800 and 1000 °C increased the crystallinity of the system and reduced the background noise. The powder corresponding to nominal

Table 1. Position Coordinates of Various Atoms in Representative $Sm_{1-x}Dy_xZr_2O_7$ (x = 0.0, 0.6, and 1.8)

	X	Y	Z	occ.
		$Sm_2Zr_2O_7$		
O1	0.3482	0.1250	0.1250	1.0000
O2	0.3750	0.3750	0.3750	1.0000
Zr	0.0000	0.0000	0.0000	1.0000
Sm	0.5000	0.5000	0.5000	1.0000
		$Sm_{1.4}Dy_{0.6}Zr_2O_7$		
O1	0.3563	0.1250	0.1250	1.0
O2	0.3750	0.3750	0.3750	1.0
Zr/Sm	0.0000	0.0000	0.0000	0.54(2)/0.46(2)
Sm/Dy/Zr	0.5000	0.5000	0.5000	0.24(2)/0.3/0.56(2)
		$Sm_{0.2}Dy_{1.8}Zr_2O_7$		
O	0.2500	0.2500	0.2500	0.875
Sm	0.0000	0.0000	0.0000	0.05
Dy	0.0000	0.0000	0.0000	0.45
Zr	0.0000	0.0000	0.0000	0.50

dx.doi.org/10.1021/ic200108u |*Inorg. Chem.* 2011, 50, 2354–2365

Table 2. Crystallographic Data and Structure Refinement Parameters of $Sm_{1-x}Dy_xZr_2O_7$ (x = 0.0, 0.6, and 1.8)

	$Sm_2Zr_2O_7$	$Sm_{1.4}Dy_{0.6}Zr_2O_7$	$Sm_{0.2}Dy_{1.8}Zr_2O_7$
space group	$Fd\bar{3}m$	$Fd\bar{3}m$	$Fm3m$
a (Å)	10.6305(2)	10.4187(3)	5.2421(3)
V (Å^3)	1201.31(4)	1130.95(5)	144.05(5)
Z	8	8	4
profile parameter			
u	2.095	2.577	0.455
v	−0.918	−0.850	−0.182
w	0.187	0.149	0.087
η_0	0.160	0.160	0.049
GOF (χ^2)	5.83	1.93	2.37
R_p, R_{wp}, R_{exp}	10.8, 15.2, 6.28	5.87, 7.8, 5.62	6.88, 9.22, 5.99
R_B	9.44	3.01	5.64

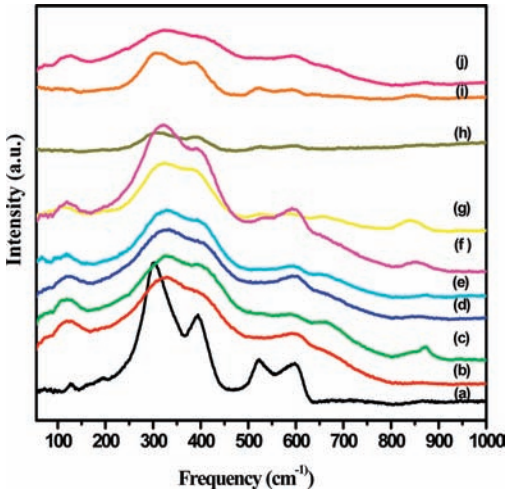

Figure 2. Raman spectra of $Sm_{1-x}Dy_xZr_2O_7$, where x is (a) 0.0, (b) 0.20, (c) 0.40, (d) 0.60, (e) 0.80, (f) 1.0, (g) 1.4, (h) 1.6, (i) 1.8, and (j) 2.0.

composition, pure $Sm_2Zr_2O_7$, sintered at 1450 °C showed the XRD pattern typical of a pyrochlore lattice with superlattice peaks at $2\theta \approx 14°$ (111), 27° (311), 29° (222), 34° (400), 37° (331), 45° (511), etc., as shown in Figure 1A. These pyrochlore-type peaks were retained until 40 mol % Dy^{3+} concentration, albeit with decreasing intensity of the superstructure peaks. Beyond 40 mol % Dy^{3+}, the disappearance of the pyrochlore-type superstructure peaks was observed. The typical XRD patterns in this series are shown in Figure 1. The cell parameters for each nominal composition, along with both end members, were refined using *POWDERX*. Variation of the lattice parameter as a function of the Dy^{3+} content is presented in Figure 1B. Structural analysis has been done by using the Rietveld refinement program *Fullprof-2005*.[37] The Rietveld refinement was started with an appropriate structural model and an approximate scale parameter. The background was fitted with a sixth-order polynomial function. The peak profile was fitted with a pseudo-Voigt profile function. Subsequently, positional parameters were refined with an overall thermal parameter. The typical refined parameters are summarized in Tables 1 and 2. The fitted plot of $Sm_{1.4}Dy_{0.6}Zr_2O_7$ is shown in Figure I(C) as a representative of the compositions.

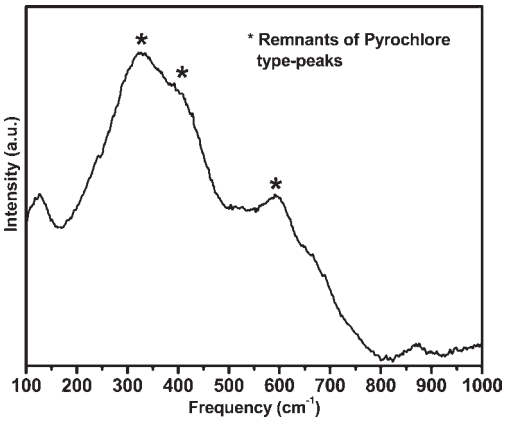

Figure 3. Raman spectrum of $Dy_2Zr_2O_7$.

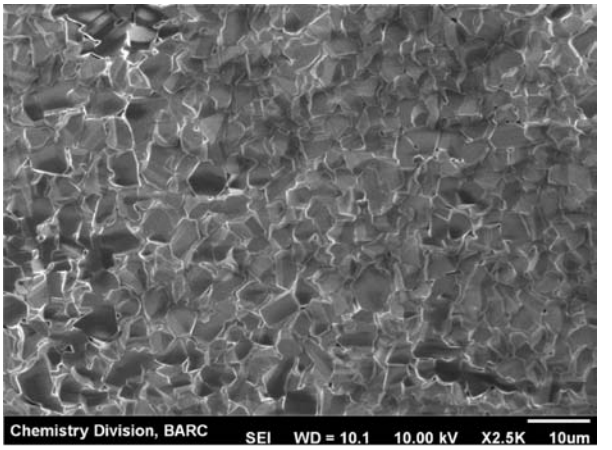

Figure 4. SEM image of $Sm_{1.4}Dy_{0.6}Zr_2O_7$ pellet-sintered at 1450 °C.

Figure 2 depicts the Raman spectra of $Sm_{2-x}Dy_xZr_2O_7$ wherein the peaks successively broaden upon Dy^{3+} addition. Figure 3 gives the Raman spectrum of the nominal composition $Dy_2Zr_2O_7$.

A scanning electron microscopy (SEM) image was recorded on the top planar surface of the sintered specimen of representative composition $Sm_{1.4}Dy_{0.6}Zr_2O_7$ and is presented in Figure 4. The sample consists of dense regularly shaped grains. The density was found to be ~95% of the theoretical density.

Electrical conductivities of a few representative samples were evaluated from the measured impedance plot at each temperature. The typical impedance spectra in the form of Nyquist plots (Cole−Cole plots) recorded on $Sm_2Zr_2O_7$, $Sm_{0.8}Dy_{1.2}Zr_2O_7$, and $Dy_2Zr_2O_7$ samples at different temperatures are shown in Figure 5. The individual semicircular portions of each impedance spectrum were fitted into an equivalent parallel resistance-capacitance (RC) circuit model, typical for semicircular behavior in impedance spectroscopy[38,39] using the *Zview 2.9b* software, and the component resistance and capacitance values were estimated for the corresponding regions, i.e., bulk (R_b and C_b), grain boundary (R_{gb} and C_{gb}), and electrode polarization regions (R_{el} and C_{el}) of the sample. The overall impedance response of the samples was fitted as a series connection of these individual parallel RC circuit elements. As is generally observed for most oxide ion conductors, impedance response due to different regions (bulk and grain boundary) of these samples was found to partially overlap the frequency sweep region (as is clearly visible from the Nyquist plot in Figure 5). Therefore, the total

dx.doi.org/10.1021/ic200108u |*Inorg. Chem.* 2011, 50, 2354–2365

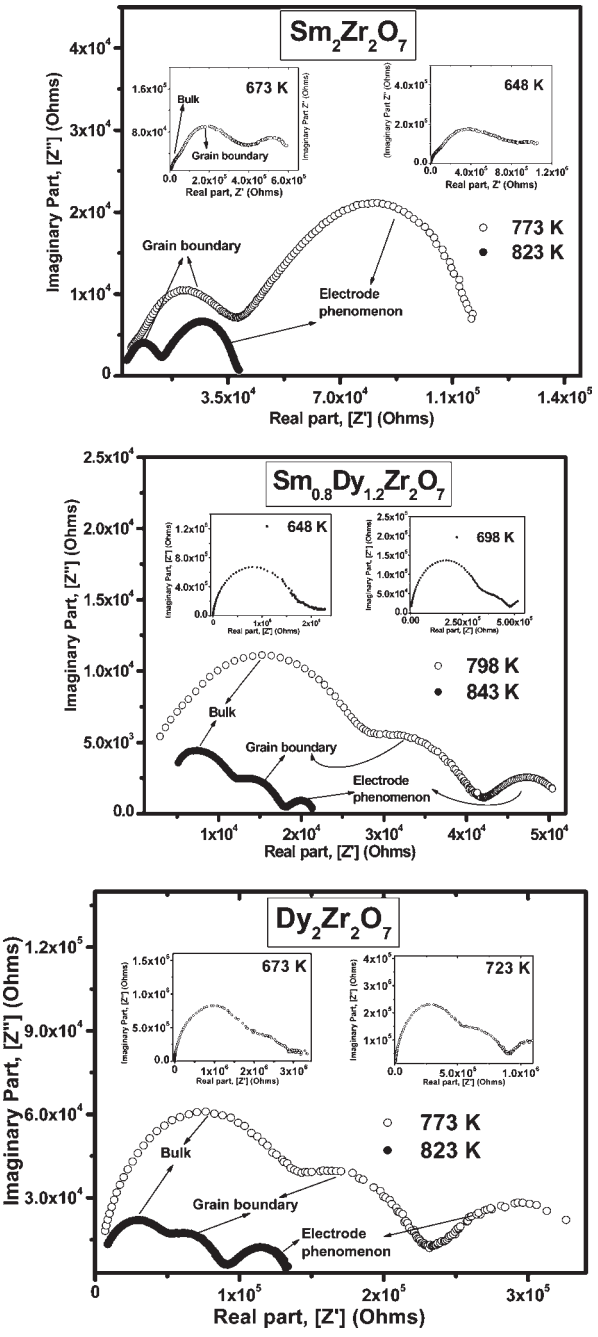

Figure 5. Representative Nyquist plots for $Sm_2Zr_2O_7$, $Sm_{1.2}Zr_{0.8}O_7$, and $Dy_2Zr_2O_7$ compositions.

resistance of the sample, R_t, at a given temperature was taken as the intercept of the grain boundary impedance response arc on the Z' axis toward the lower-frequency region.

The total electrical conductivity of the samples as a function of the temperature, i.e., $\sigma_t(T)$, was evaluated using the total resistance (R_t), calculated at each temperature for all of the samples and cell constants (cell constant = l/a, calculated from the circular surface area A and the thickness l of the samples). Figure 6 shows the temperature dependence of the total electrical conductivity of samples $Sm_2Zr_2O_7$, $Sm_{1.2}Zr_{0.8}O_7$, and $Dy_2Zr_2O_7$ in the form of Arrhenius plots.

Discussion. The XRD pattern observed for $Sm_2Zr_2O_7$ (Figure 1a) was ascribed to the pyrochlore phase, and its lattice parameter was calculated to be 10.594 Å, which is in agreement with that reported in the literature (JCPDS card no. 24-1012; space group $Fd3m$). It was observed that the intensity of the superlattice peaks decreased with an increase in the Dy^{3+} concentration, and finally the XRD pattern showed the disappearance of these peaks after 40 mol % Dy^{3+} doping. Referring to the literature, it has been reported that observation of the pyrochlore lattice, $A_2B_2O_7$, is dependent on the r_A/r_B ratio. The radius ratio for $Sm_2Zr_2O_7$ is calculated to be 1.50 [$r(Sm^{3+})$ = 1.079 Å; $r(Zr^{4+})$ = 0.72 Å], whereas the radius ratio for $Dy_2Zr_2O_7$ is 1.43 [$r(Dy^{3+})$ = 1.027 Å]. The ionic radii are taken in 8-fold coordination for Sm^{3+} and Dy^{3+} and 6-fold coordination for Zr^{4+}.[40] Thus, $Sm_2Zr_2O_7$ is within the limiting radius ratio required for stabilization of the pyrochlore structure, whereas $Dy_2Zr_2O_7$ has the radius ratio in the defect fluorite regime. Hence, with an increase in the Dy^{3+} content at the A site, there is an increased tendency to transform from an ordered pyrochlore lattice to a disordered fluorite lattice. In fact, in the nominal composition $Sm_{1.2}Dy_{0.8}Zr_2O_7$, the radius ratio is 1.46, which is just the borderline value for observing a pyrochlore-type lattice. Hence, this further supports the disappearance of superstructure peaks beyond this composition. Alternately, as the radius ratio decreases, the difference in the sizes of two cations decreases and, consequently, the ease of cation antisite formation increases, thereby resulting in the loss of cation ordering. When the cations are different in size, the A-site cation assumes 8-fold coordination, the smaller B-site cation assumes 6-fold coordination, and the structure that results is based on a fluorite-type structure, except that there is a periodic arrangement of the oxygen vacancy. This ordered arrangement tends to disorder in the case of the cationic sizes becoming similar. The oxygen vacancy is statistically distributed over all of the sites, and we get a fluorite-type lattice. Also, the lattice parameter was found to decrease with an increase in the Dy^{3+} concentration. On the basis of the relative ionic size considerations, one can explain the decrease in the lattice parameter of both pyrochlore- and fluorite-type modifications upon incorporation of Dy^{3+} ions at the Sm^{3+} sites. Figure 1B graphically depicts variation of the lattice parameter with the Dy^{3+} content. A change in the slope at 40 mol % Dy^{3+} substitution indicates a change in the structural features.

Because XRD gives an average structure because of the inherent nature of the technique, these systems were also studied using Raman spectroscopy to investigate whether ordering is retained at the microdomain levels despite the apparent disorder existing in these systems, as shown by powder XRD. It is well-known that XRD studies are more sensitive to disorder on the cationic sublattice compared to the anionic sublattice, whereas Raman spectroscopy is primarily sensitive to oxygen-cation vibrations and hence is an excellent probe for studying the local disorder. Further, there have been examples wherein Raman spectroscopic investigations provide unequivocal information[25] to distinguish between a defect fluorite structure and the so-called pyrochlore structure for compositions with the radius ratio lying at the borderline of the pyrochlore and defect fluorite.

The fluorite structure is known to possess only one Raman-active mode (T_{2g}). The Raman spectrum of the fluorites has a single broad band because all O ions in the fluorite structure are randomly distributed over the eight total available anion sites and hence are equivalent. This gives rise to disorder, and because of this, the Raman spectrum is reduced to a broad continuum of density of states (DOS). On the other hand, the Raman spectrum of a pyrochlore structure has six Raman-active modes according

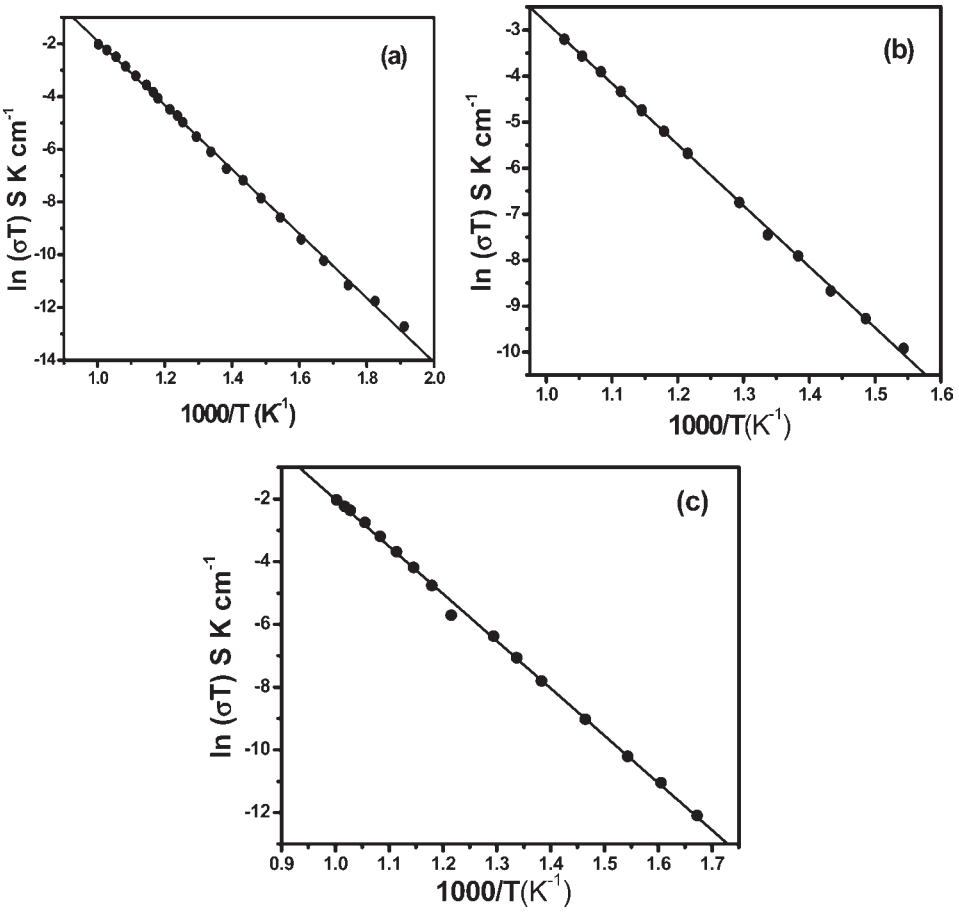

Figure 6. Arrhenius plots for $Sm_{1-x}Dy_xZr_2O_7$, where x is (a) 0.0, (b) 1.2, and (c) 2.0.

to group theory, which are

$$\Gamma = A_{1g} + E_g + 4T_{2g}$$

The Raman spectrum recorded on $Sm_2Zr_2O_7$ is displayed in Figure 2. According to the polarized Raman measurements reported in the literature,[41,42] the Raman band at 520 cm^{-1}, which can display significant intensity changes with different polarization directions, is assigned to the A_{1g} mode and it is said to be majorly due to O−B−O bending. The band with the maximum intensity (~300 cm^{-1}) is assigned to the E_g mode. It is due to the B−O_6 bending vibrations. The bands observed at 394 cm^{-1} (mostly B−O stretching with contributions from A−O stretching and O−B−O bending) and 595 cm^{-1} (mostly B−O stretching) were assigned to two of the four T_{2g} modes. A relatively weak band, observed at 125 cm^{-1}, can be associated with anharmonic effects or disorder in the material, as was also reported by Vandenborre et al.[41]

It is observed that the sharp Raman features observed in pure $Sm_2Zr_2O_7$ broaden enormously with Dy^{3+} substitution (Figure 2). Because the samples were subjected to high temperatures (1450 °C), this broadening cannot be attributed to the smaller sizes of the particles. It is known that the presence of the vacancies, defects, and foreign ions in the ordered lattice disrupts the translational symmetry and, consequently, it relaxes the $k = 0$ selection rule. Phonons from all parts of the Brillouin zone, therefore, contribute to the optical spectra, thereby resulting in broad bands.[42] Therefore, substitution of a foreign ion (Dy^{3+}) in $Sm_2Zr_2O_7$ is the cause for the broadening of Raman features.

Glerup et al.[25] observed that when a cation disorder is introduced in $Y_2Ti_2O_7$ by substituting Ti^{4+} with Zr^{4+}, the Raman mode observed around 531 cm^{-1} loses intensity and becomes broader as the concentration of the dopant is increased. The corresponding mode in zirconates appears around ~520 cm^{-1}. A similar observation can be made from Figure 2, wherein the introduction of even 10 mol % Dy^{3+} causes the peak at 520 cm^{-1} to diminish significantly relative to other peaks. Also, careful analysis of the Raman spectrum (Figure 2) reveals that, even with the onset of substitution of Dy^{3+}, the main peak at ~300 cm^{-1} undergoes a significant broadening, whereas the relative intensity of the peak at ~394 cm^{-1} does not change much. Factor Group analysis shows[43] shows that the T_{2g} mode associated with the 394 cm^{-1} peak involves the 8b oxygen atom in the pyrochlore structure, whereas the other three T_{2g} modes are associated with the 48f oxygen atoms. Considering that the broadening of Raman lines is due to disorder or strain in the lattice, this clearly indicates that, upon Dy^{3+} substitution, 48f oxygen atoms undergo significant disorder, whereas the 8b oxygen atom is virtually undisturbed by this substitution. Qu et al. have observed similar behavior in $Sm_2Zr_2O_7$ doped with MgO.[38] Identical changes have been reported by Mandal et al. in $Nd_{2-y}Y_yZr_2O_7$ system.[44] Further, the changes in the frequencies of different modes were plotted with the Dy^{3+} content, and it was found that there is no discernible change in the peak positions with a change in the composition (figure not included). This observation points toward the fact that it is primarily due to involvement of oxygen ion movement and not due to the cations.

dx.doi.org/10.1021/ic200108u |*Inorg. Chem.* 2011, 50, 2354–2365

An interesting and worth-mentioning observation is that, howsoever broad, the pyrochlore features are still distinguishable by their presence in the Raman spectrum for the nominal composition $Dy_{0.5}Zr_{0.5}O_{1.75}$ (or $Dy_2Zr_2O_7$; Figure 3). Also, the single band observed at ~466 cm^{-1}, typical of the fluorite-structured oxides,[45] was not observed in this study. Moreover, the absence of C-type Sm_2O_3 bands at 344, 417, and 465 cm^{-1} and C-type Dy_2O_3 bands at 334 and 372 cm^{-1} eliminates the presence of the C-type phase as well. It has been reported,[46,47] based on XRD studies, that $Dy_{0.5}Zr_{0.5}O_{1.75}$ (or $Dy_2Zr_2O_7$) is a defect fluorite with complete disorder of the metal ions and oxygen vacancies. The same has been observed in the powder XRD pattern of this composition (Figure 1a), wherein no superstructure peaks corresponding to pyrochlore were observed; in fact, they are found to disappear much before, at around 40 mol % of Dy^{3+} substituted for Sm^{3+}. However, as mentioned above, the Raman spectrum of $Dy_2Zr_2O_7$ (Figure 3) still shows the remnants of pyrochlore-type ordering. On this basis, it can possibly be deduced that, even though a substantial disorder is present in the $Dy_2Zr_2O_7$ lattice, the order is still present at the microdomain levels, which could be detected by Raman spectroscopy. Similar weak ordering was also observed earlier by Mandal et al.,[48] wherein $Dy_2Hf_2O_7$, which is expected to be a defect fluorite, exhibits weak peaks corresponding to the pyrochlore structure in the Raman spectrum. Therefore, from a combination of the XRD and Raman spectroscopic studies, it can be inferred that, upon Dy^{3+} substitution in $Sm_{2-x}Dy_xZr_2O_7$, the system makes a transition from a perfect pyrochlore lattice to a disordered pyrochlore lattice. However, in the Dy^{3+}-rich region, whether to call it a defect pyrochlore (as suggested by Raman spectroscopy) or a defect fluorite (as suggested by XRD studies) remains a question. A plausible explanation could be to define it as having weakly ordered pyrochlore microdomain regions in the bulk defect fluorite lattice.

To investigate the correlation between induced disorder and conductivity, the given pyrochlore systems, $Sm_{2-x}Dy_xZr_2O_7$, were subjected to ionic conductivity studies. Dense pellets (~95% of the theoretical density) were made for the ionic conductivity studies. The representative SEM image is shown in Figure 4. Figure 5 shows a Nyquist plot of the specific impedance [the imaginary part, $Z''(w)$, versus the real part, $Z'(w)$] for $Sm_2Zr_2O_7$, $Sm_{0.8}Dy_{1.2}Zr_2O_7$, and $Dy_2Zr_2O_7$ samples at different temperatures as representative data of all of the samples analyzed. One can observe the characteristic semicircles found in these kinds of plots for polycrystalline ionic conductors, which include one component due to the bulk response at the highest frequencies and a second one at the lowest frequencies, which is related to the grain boundary response. The incomplete semicircle arc at lower frequencies can be ascribed to the impedance associated with the sample−electrode interface (electrode polarization).[39] Upon an increase in the temperature, this ion-blocking effect becomes more and more prominent due to ions accumulating at the electrodes (Figure 5). Both R_b (bulk resistance) and R_{gb} (grain boundary resistance) showed a decreasing trend with an increase in the temperature. Similar behavior is observed for all other samples also.

Variation of the conductivity with temperature (Arrhenius equation) for all of these compositions (Figure 6) exhibits a fairly good linear relationship between $\ln(\sigma_t T)$ and $1000/T$. The values of the activation energy of ionic conduction E_a and the preexponential factor σ_0 for each sample were obtained from the slopes and intercepts of the linear fit of the above plots, respectively. Table 3 summarizes the results of this analysis. It can be seen that the activation energy of ionic conduction increases with a change in the composition from pure $Sm_2Zr_2O_7$ (1.049 eV) with increasing Dy^{3+} substitution and is maximum for pure $Dy_2Zr_2O_7$ (1.298 eV) (Figure 7). A similar increasing trend is observed in variation of the preexponential factor with an increase in the Dy^{3+} content. Considering the fact that the one of the parent compounds in the present system, namely, $Sm_2Zr_2O_7$ is a perfectly ordered pyrochlore, whereas the other end member $Dy_2Zr_2O_7$ is a system with a significant amount of disorder in it, it is clear that the addition of more and more Dy^{3+} into $Sm_2Zr_2O_7$ increases the degree of disorder into the pyrochlore structure, thus causing decreased oxygen ion mobility. This, in turn, results in an increase in the energy of activation of ionic conduction with increased Dy^{3+} content. Various calculations have been performed on similar kinds of systems, and it has been shown that, in the ordered structure, there are preferential diffusion paths through the cation tetrahedra around the 48f oxygen sites and these should lead to a decrease in the strain energy contribution to the activation enthalpy for conductivity, thus yielding lower activation energies and higher conductivities upon ordering.[49] The increase in the conductivity, upon ordering, particularly in the case of A-site doping, has also been explained in terms of an increase in the unit cell volume. It has been shown that, in fluorite and pyrochlore $Ln_2Zr_2O_7$ lanthanide zirconates, the cell volume is linearly dependent on the ionic radius of the A-type cation.[50] A larger unit cell volume makes it easier for the mobile species to migrate, and hence there is, consequently, a lower energy barrier for mobile oxygen ions.[28] An increasing trend in the value of the

Table 3. Variation of Activation Energies (E_a) and Preexponential Factors with the Composition

sample	E_a (eV)	preexponential factor σ_0(S cm^{-1} K)
$Sm_2Zr_2O_7$	1.049	1.028×10^4
$Sm_{1.8}Dy_{0.2}Zr_2O_7$	1.052	1.149×10^4
$Sm_{1.2}Dy_{0.8}Zr_2O_7$	1.144	1.045×10^4
$Sm_{0.8}Dy_{1.2}Zr_2O_7$	1.168	1.196×10^4
$Sm_{0.4}Dy_{1.6}Zr_2O_7$	1.190	1.198×10^4
$Dy_2Zr_2O_7$	1.298	1.306×10^4

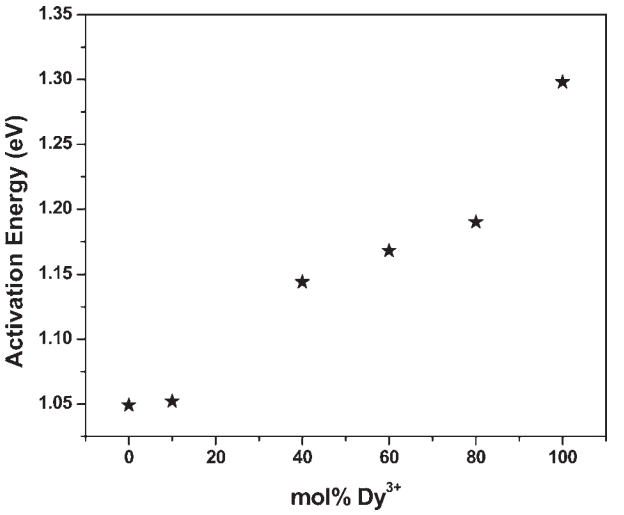

Figure 7. Variation of E_a (activation energy) for $Sm_{1-x}Dy_xZr_2O_7$ with the Dy^{3+} content.

dx.doi.org/10.1021/ic200108u |Inorg. Chem. 2011, 50, 2354–2365

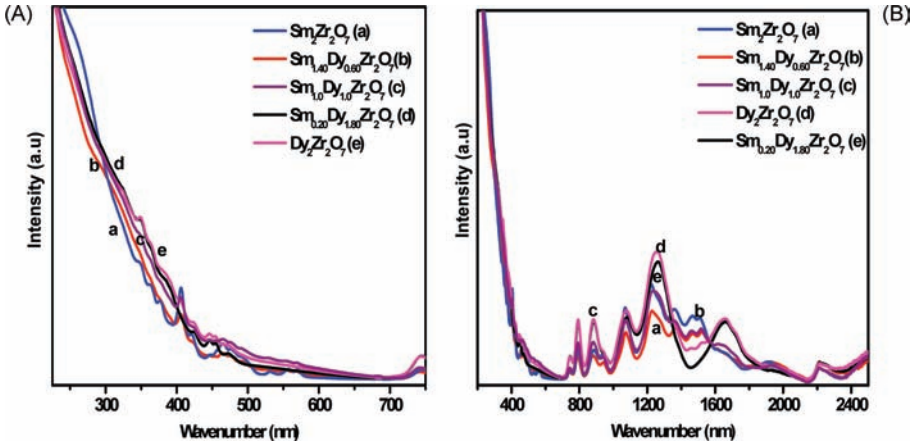

Figure 8. DR-UV spectra of $Sm_{1-x}Dy_xZr_2O_7$ where x is (a) 0.0, (b) 0.30, (c) 0.50, (d) 0.9, and (e) 2.0 in the wavelength ranges (A) 200−600 nm and (B) 200−2400 nm.

preexponential factor σ_0 with an increase in the Dy^{3+} content (Table 3) suggests an increase in the concentration of mobile species (O^{2-} ions), which is known to increase as a function of the degree of disorder in the system.[44]

Another interesting observation is that, although the total ionic conductivity of samples in $Sm_{2-x}Dy_xZr_2O_7$ decreases with an increase in the Dy^{3+} content, there is a distinct rise in the conductivity with an initial 10 mol % doping of Dy^{3+}, i.e., in the nominal composition $Sm_{1.9}Dy_{0.1}Zr_2O_7$. It is observed that there is a marked increase in the preexponential factor of this composition, although the decrease in E_a is nominal. Thus, there are two factors that are operating in the system with the introduction of Dy^{3+} ions in the $Sm_2Zr_2O_7$ lattice, i.e., an increase in the number of mobile species due to an increase in disorder and an increase in resistance offered to the migrating ions due to an increase in disorder. Both of these factors are competing and, hence, control variation in the total conductivity of the system. Probably, the decrease in the conductivity brought about by an increase in resistance to the motion of ions by enhanced disorder is more than offset by an increase in the number of charge carriers upon moving from $Sm_2Zr_2O_7$ to $Sm_{1.9}Dy_{0.1}Zr_2O_7$, which might explain the initial rise in the conductivity from $Sm_2Zr_2O_7$ to $Sm_{1.9}Dy_{0.1}Zr_2O_7$.

3.2. DR-UV and Photocatalytic Studies. There has been a growing interest in pyrochlores for their applications in photocatalysis. For a material to act as a photocatalyst, it should have an appropriate band gap to enable it to absorb effectively. For this purpose, band-gap measurements were performed on the $Sm_{2-x}Dy_xZr_2O_7$ system. Parts A and B of Figure 8 represent the DR UV−visible spectra of the $Sm_{2-x}Dy_xZr_2O_7$ system in different wavelength ranges. With an increase in Dy^{3+} substitution in $Sm_2Zr_2O_7$ (Figure 8A, curves b−e), the respective band gaps exhibit red shifts compared to undoped $Sm_2Zr_2O_7$ (curve a), and this shift is found to increase with an increase in the Dy^{3+} content. Thus, the band gap decreases with an increase in the Dy^{3+} content. Despite a decrease in the band gap, the major absorbance of these catalysts still lies in the UV region. The "indirect band gaps" are calculated using $\alpha^{1/2}$ (indirect transition allowed), where α is

$$\alpha \propto \frac{(h\nu - E_g + E_p)^2}{\exp\left(\frac{E_p}{kT}\right) - 1} + \frac{(h\nu - E_g + E_p)^2}{1 - \exp\left(\frac{E_p}{kT}\right)}$$

Table 4. Variation of the Band Gap and $t_{1/2}$ with the Composition

sample	band gap (eV)	$t_{1/2}$ (min)
$Sm_2Zr_2O_7$	3.81	3.4
$Sm_{1.4}Dy_{0.6}Zr_2O_7$	3.62	4.5
$Sm_{1.0}Dy_{1.0}$ Zr_2O_7	3.58	5.5
$Sm_{0.2}Dy_{1.8}Zr_2O_7$	3.45	11.84
$Dy_2Zr_2O_7$	3.44	14.81

Here, E_p is the energy of the phonon that assists in the transition, k is Boltzmann's constant, T is the thermodynamic temperature, α is the absorption coefficient, ν is light frequency, and h is Planck's constant. The system is found to possess a tunable band gap, which varies from ~3.84 to 3.45 eV upon a gradual change in the composition from pure $Sm_2Zr_2O_7$ to pure $Dy_2Zr_2O_7$ in the present systems (Table 4). Because all of the samples were heated at higher temperature (1450 °C), lowering of the band gap cannot be attributed to the particle size effect.

Theoretical studies using the first-principles calculations were performed on this system to understand the lowering of the band gap with the extent of Dy^{3+} doping. First-principles local density approximation (LDA) based tight-binding linear muffin-tin orbital (TB-LMTO) calculations were performed to understand the role played by Dy^{3+} dopant ions in modifying the electronic structure and thus the photocatalytic properties of $Sm_2Zr_2O_7$. The self-consistent scalar relativistic TB-LMTO method within the atomic sphere approximation (ASA) was employed, which also included the so-called "combined correction" term.[51−53] The potential is calculated using the density functional theory prescription under the LDA. Von Barth−Hedin parametrization of the exchange-correlation potential was employed for this purpose. Further, the tetrahedron method of Brillouin zone (k-space) integration was used.[53] It should be pointed out here that in spite of the fact that the TB-LMTO-ASA method does not include spin−orbit effects, which may become important for heavier elements ($Z > 50$), the method is well-known to produce qualitative features of the band structure quite accurately.

Three structures, (i) a pyrochlore $Sm_2Zr_2O_7$ ($Fd\bar{3}m$), (ii) a pyrochlore-based supercell (SC1) having $Sm_{11}Dy_5Zr_{16}O_{56}$ composition and doped with 31.25 atom % Dy occupying the Sm sites, and (iii) a fluorite-based supercell (SC2) having $Dy_2Zr_2O_7$ composition, were considered for this study (Figure 9). The unit

dx.doi.org/10.1021/ic200108u |Inorg. Chem. 2011, 50, 2354–2365

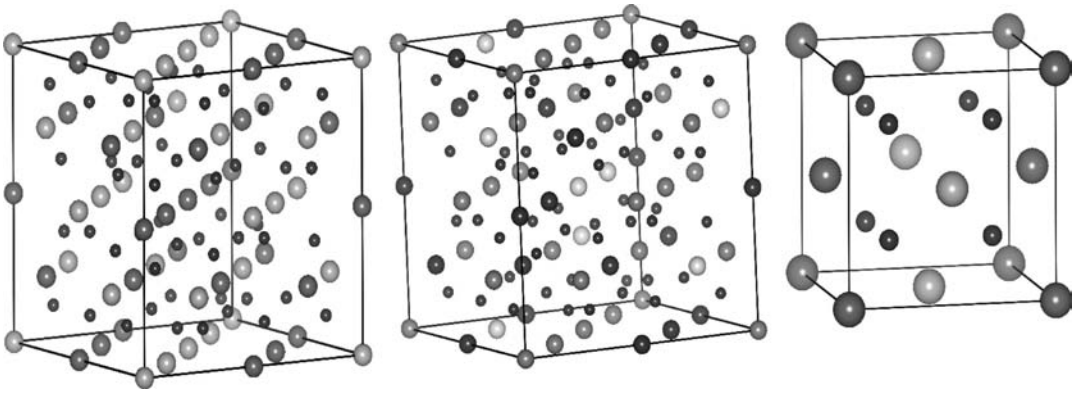

Figure 9. Unit cells of (a) pyrochlore $Sm_2Zr_2O_7$ (*Fd*3; big dark circles, Sm; big gray circles, Zr; small black circles, O), (b) pyrochlore-based supercell (SC1) $Sm_{11}Dy_5Zr_{16}O_{56}$ having 31.25% Dy doping (big black circles, Sm; big gray circles, Zr; big light-gray circles, Dy; small black circles, O), and (c) fluorite-based supercell $Dy_2Zr_2O_7$ (big dark circles, Dy; big gray circles, Zr; small black circles, O).

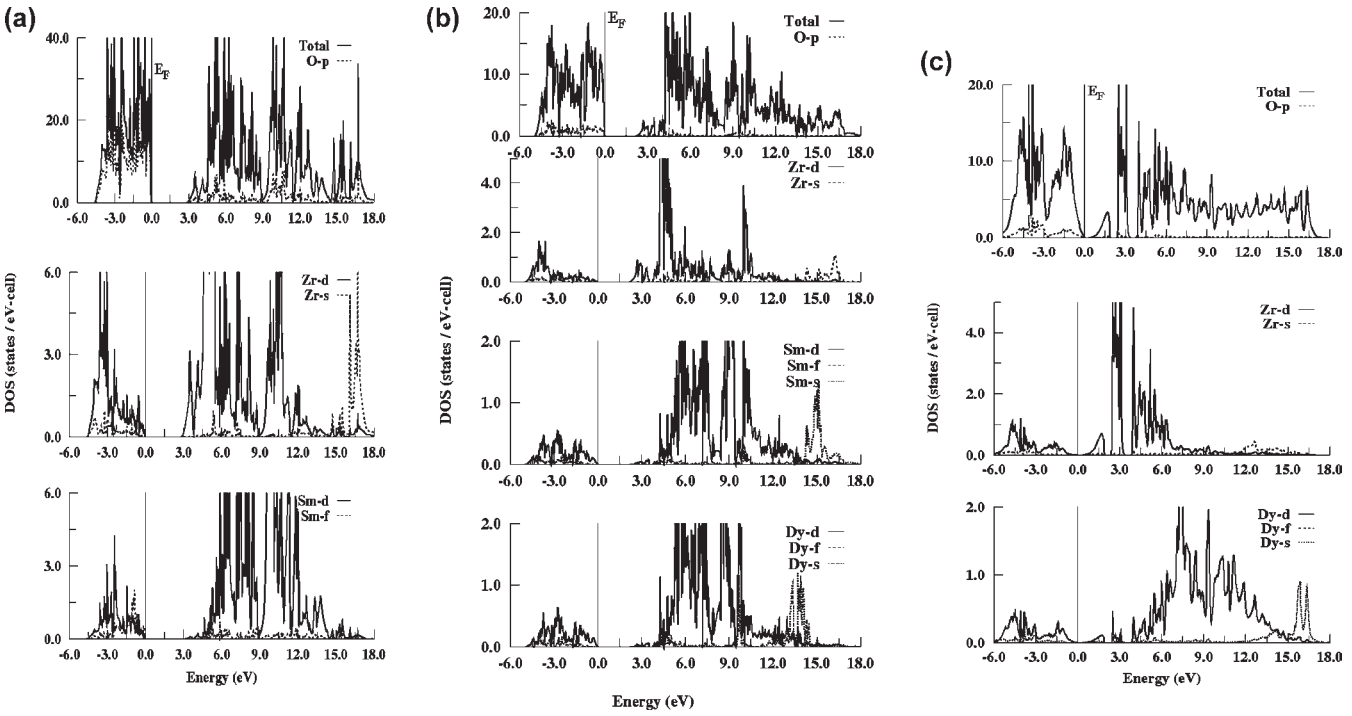

Figure 10. Total as well as site- and angular-momentum-projected DOS for (a) pyrochlore $Sm_2Zr_2O_7$, (b) pyrochlore-based supercell (SC1) $Sm_{11}Dy_5Zr_{16}O_{56}$ having 31.25% Dy doping, and (c) fluorite-based supercell $Dy_2Zr_2O_7$.

cell of $Sm_2Zr_2O_7$ contained 22 atoms, from which a primitive 1 × 1 × 1 supercell (SC1) containing 88 atoms (Sm, 16; Zr, 16; O, 56) was generated. Of these 16 Sm atoms, 5 atoms were randomly substituted by Dy, leading to a $Sm_{11}Dy_5Zr_{16}O_{56}$ composition for SC1. The fluorite-based supercell, SC2, was obtained from a fluorite structure (Dy_4O_8) by generating a primitive 1 × 1 × 1 supercell and randomly replacing two of the Dy sites by Zr and removing an O atom. Spin-averaged LDA calculations were performed on these structures. The basis set consisted of 6s and 5d states of Sm and Dy, 5s, 5p, and 4d states of Zr, and 2p states of O, while 4f states of Zr, 3s and 3d states of O, and 6p states of Sm and Dy were downfolded,[54] thereby restricting the size of the Hamiltonian and overlap matrices without sacrificing the accuracy of the results. For empty spheres, only the 1s states were included, downfolding the p and d states. All calculations are fully converged with respect to the number of *k* points.

Parts a−c of Figure 10 show the total as well as site- and *l-projected* partial DOS for $Sm_2Zr_2O_7$, SC1, and SC2, respectively. As can be seen in Figure 10a, the total DOS exhibits a band gap of 2.92 eV between the fully filled valence band and the empty conduction band. The calculated band gap is not in good agreement with the measured value of 3.84 eV. This can result from the nature of the LDA method used and the band structure of $Sm_2Zr_2O_7$. The valence band exhibits a strong mixing of O p, Zr d, and Sm d and f states. Close to the Fermi energy, O p states make a strong contribution to the valence band, and the band gap arises mainly between these O p and the antibonding Zr d states in the conduction band. The conduction band also has contributions from the Sm d and f states. Figure 10b depicts the total as well as site- and *l-projected* partial DOS for the Dy-doped structure (SC1). The calculated band gap is about 2.25 eV, which is lower than that for the undoped pyrochlore. As can be

dx.doi.org/10.1021/ic200108u |*Inorg. Chem.* 2011, 50, 2354–2365

seen in Figure 10b, the effect of the Dy addition seems to have caused a further splitting of mainly the Zr d states in the conduction band, thereby creating a small band, now a conduction band, with a bandwidth of ~2.00 eV in the middle. Moreover, the valence band has a strong contribution from Dy d states near the Fermi energy, with some contributions coming from the O p and Sm d states. The Dy and Sm f states have been pushed to higher binding energy in the valence band, pushing the d states to higher energy and reducing the gap between the filled bonding and unfilled antibonding states, thereby reducing the band gap. The DOS plots for a fluorite-based supercell (SC2) exhibit an even smaller band gap of only 0.6 eV (see Figure 10c), which, however, is not consistent with the measured value of 3.45 eV. As mentioned earlier, the calculated band gap can have large errors depending upon the nature of the LDA method used, and our TB-LMTO-ASA calculations can predict qualitative features quite accurately. The SC2 supercell has no Sm in it. The band gap in the DOS plots of the SC2 supercell mainly arises from the splitting of filled bonding and unfilled antibonding Dy and Zr d states. The Dy f states lie on the higher binding energy in the valence band, which also has a strong contribution coming from O p states near the Fermi energy. The unfilled Dy and Zr d states exhibit further splitting in the conduction band, which exhibits three sub-bands compared to two in the DOS plots for the SC1 supercell. These calculations explain the observed decreasing trend of the band gap in this series as a function of the Dy^{3+} content.

Photocatalysis. In order to explore the potential of this system as a photocatalyst in UV-based photocatalysis, representative nominal compositions, viz., pure $Sm_2Zr_2O_7$ and $Dy_2Zr_2O_7$, the middle composition $Sm_{1.0}Dy_{1.0}Zr_2O_7$, as well as one composition each from the Dy-rich region ($Sm_{0.2}Dy_{1.8}Zr_2O_7$) and the Sm-rich region ($Sm_{1.4}Dy_{0.6}Zr_2O_7$), respectively, were subjected to dye degradation studies. The degradation of xylenol orange was taken as the model reaction to test the photocatalytic activity of this system. Xylenol orange has the following structure at neutral pH.

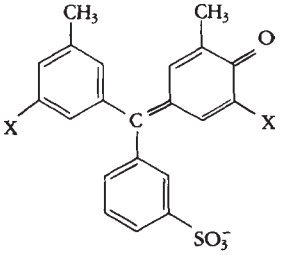

X = $CH_2NCCH_2COOH)_2$

The UV−visible spectra of the xylenol orange dye solution shows absorbance peaks at 275 and 430 nm in agreement with that reported in the literature.[55] Interestingly, when catalysts ($Sm_{2-x}Dy_xZr_2O_7$) are added to the dye solution, the UV−visisble spectra exhibited a new peak at 570 nm, which could be due to the electronic interaction of dye and the catalyst (Figure 11). This new peak (570 nm) was observed for all of the compositions studied. The color of the dye solution also changed from the original yellowish-orange to pink upon the addition of a catalyst. This also indicates interaction of the dye with the catalyst. In the $Sm_{2-x}Dy_xZr_2O_7$ series, the intensity of this new 570 nm peak was maximum for $Sm_2Zr_2O_7$. Interestingly, for 10 mol % Dy^{3+} substitution, the intensity of the 570 nm

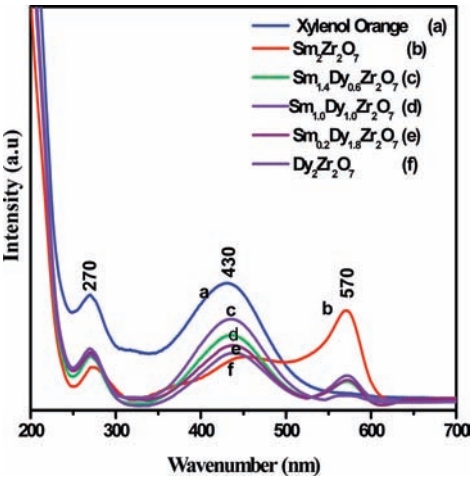

Figure 11. UV−visible spectra of (a) 10^{-5} M xylenol orange (dye) and a xylenol orange−catalyst suspension after an equilibration time of 30 min in the dark for the composition (b) $Sm_2Zr_2O_7$, (c) $Sm_{1.4}Dy_{0.6}Zr_2O_7$, (d) $Sm_{1.0}Dy_{1.0}Zr_2O_7$, (e) $Sm_{0.2}Dy_{1.8}Zr_2O_7$, and (f) $Dy_2Zr_2O_7$.

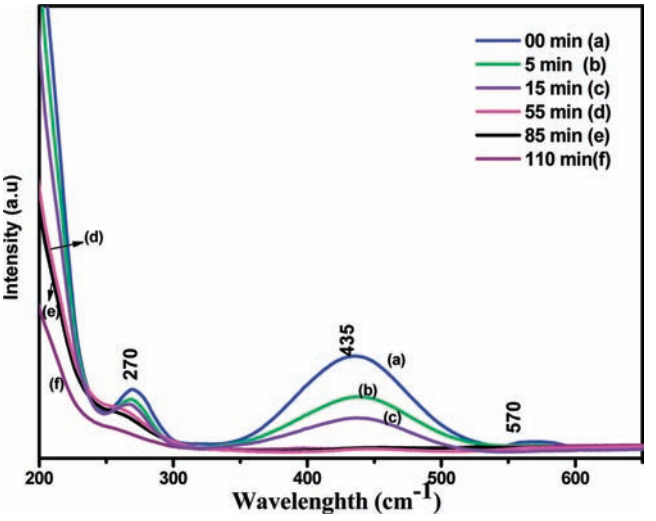

Figure 12. UV−visible spectra of the suspension of xylenol orange and $Sm_{1.4}Dy_{0.6}Zr_2O_7$ under UV irradiation as a function of time for (a) 0, (b) 5, (c) 15, (d) 55, (e) 85, and (f) 110 min, respectively.

peak decreases and then it increases gradually with and increase in the Dy^{3+} content until it reaches pure $Dy_2Zr_2O_7$. However, even for pure $Dy_2Zr_2O_7$, it is lower compared to $Sm_2Zr_2O_7$. Figure 12 shows a typical degradation profile of xylenol orange with time using the $Sm_{1.4}Dy_{0.6}Zr_2O_7$ catalyst. All of the peaks (at 570, 430, and 270 nm) were found to disappear with time, indicating that the dye is degrading in the process. Figure 13 represents the percentage product formation at different times during the course of the reaction. The $t_{1/2}$ values for the different nominal compositions as calculated from Figure 13 are tabulated in Table 4. Taking $t_{1/2}$ (time at which 50% of the dye is degraded) as a measure for the catalyst performance, it can be inferred that undoped $Sm_2Zr_2O_7$ is the most active photocatalyst for the xylenol orange degradation under UV irradiation. The value of $t_{1/2}$ increases as a function of the Dy^{3+} content in the system, which shows that they are poorer photocatalysts compared to pure $Sm_2Zr_2O_7$. Figure 14 shows variation of $t_{1/2}$ and the band gap with the Dy^{3+} content. The catalysts were subjected to

dx.doi.org/10.1021/ic200108u |*Inorg. Chem.* 2011, 50, 2354–2365

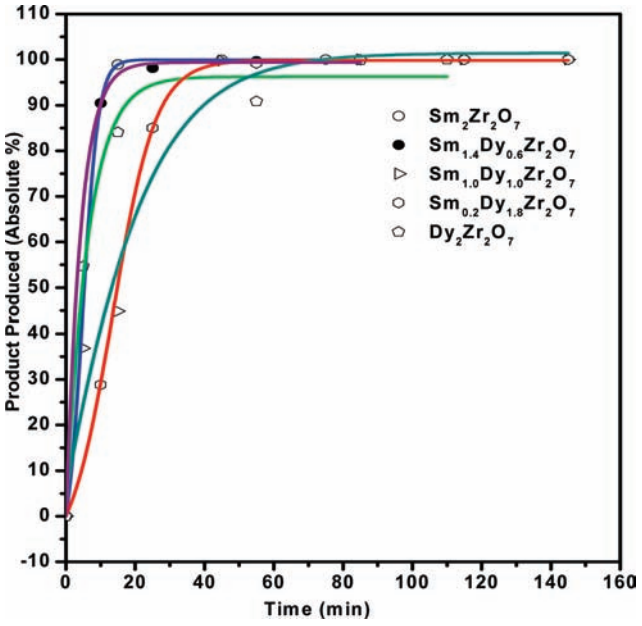

Figure 13. Plot of % product formed after degradation of xylenol orange with the catalysts (a) $Sm_2Zr_2O_7$, (b) $Sm_{1.4}Dy_{0.6}Zr_2O_7$, (c) $Sm_{1.0}Dy_{1.0}Zr_2O_7$, (d) $Sm_{0.2}Dy_{1.8}Zr_2O_7$, and (e) $Dy_2Zr_2O_7$ as a function of time.

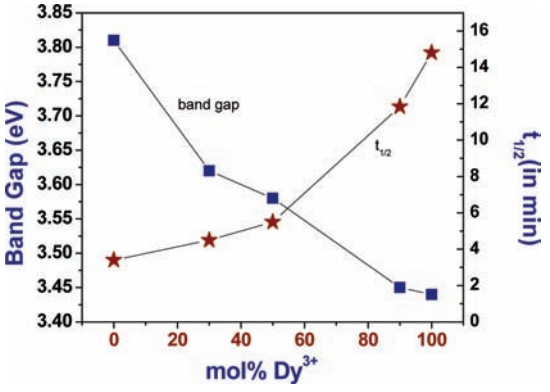

Figure 14. Variation of the band gap and $t_{1/2}$ with the Dy^{3+} content.

several cycles of the dye degradation reaction. The XRD patterns recorded on the catalysts tested for several dye degradation cycles were found to be similar to those recorded before subjecting them to the dye degradation reaction, and hence it can be concluded that they remain unchanged during the process and are stable.

4. CONCLUSIONS

This study elaborates on the detailed investigation of the $Sm_{2-x}Dy_xZr_2O_7$ ($0.0 \leq x \leq 2.0$) system with respect to its synthesis and extensive characterization by XRD and Raman spectroscopic studies and explores its multifunctionality as potential ionic conductors and also as efficient photocatalysts. The $Sm_{2-x}Dy_xZr_2O_7$ system shows complete miscibility throughout the range of compositions. The substitution of Sm^{3+} by Dy^{3+} in the pyrochlore lattice decreases the r_A/r_B ratio, thus increasing the probability of antisite formation and, hence, leading it from pyrochlore to the defect fluorite regime. However, Raman spectroscopy reveals retention of pyrochlore-type features until the other end member $Dy_2Zr_2O_7$, which can be attributed to localized ordered regions within the bulk disordered lattice. The impedance analysis on the system shows that an increase in disorder concomitant with increased Dy^{3+} content causes the activation energies (E_a) and the preexponential factors to increase. These materials have a definite band gap absorbing mainly in the UV region, which makes them good candidates for UV-based photocatalytic applications. Substituting Dy^{3+} in $Sm_2Zr_2O_7$ causes a lowering of the band gaps as a function of mol % Dy^{3+}. The theoretical studies qualitatively explain this lowering of the band gap with an increase in the Dy^{3+} content. These materials are shown to be efficient photocatalysts for degradation of xylenol orange under UV irradiation. Pure $Sm_2Zr_2O_7$ possesses the best photocatalytic properties among all of the compositions studied in this system, and the activity of these catalysts decreases as a function of the Dy^{3+} content.

AUTHOR INFORMATION

Corresponding Author

*E-mail: vinita@barc.gov.in (V.G.), aktyagi@barc.gov.in(A.K. T.). Phone: 0091-22-2559 5330. Fax: 0091-22-25505151.

ACKNOWLEDGMENT

The Department of Atomic Energy's Science Research Council is acknowledged for supporting this work via Grant 2010/21/9-BRNS.

REFERENCES

(1) Sleight, A. W. *Inorg. Chem.* **1968**, *7*, 1704.
(2) Pannetier, J.; Lucas, J. *Mater. Res. Bull.* **1970**, *5*, 797.
(3) Pruneda, J. M.; Artacho, E. *Phys. Rev. B* **2005**, *72*, 085107.
(4) Klee, W. E.; Weitz, G. *J. Inorg. Nucl. Chem.* **1969**, *31*, 2367.
(5) Sickafus, K. E.; Minervini, L.; Grimes, R. W.; Valdez, J. A.; Ishimaru, M.; Li, F.; McClellan, K. J.; Hartmann, T. *Science* **2000**, *289*, 748.
(6) Cao, X.; Vassen, R.; Fischer, W.; Tietz, F.; Jungen, W.; Stover, D. *Adv. Mater.* **2003**, *15*, 1438.
(7) Fujihara, S.; Tokumo, K. *Chem. Mater.* **2005**, *17*, 5587.
(8) Heremans, C.; Wuensch, B. J.; Stalick, J. K.; Prince, E. *J. Solid State Chem.* **1995**, *117*, 108.
(9) Raju, N. P.; Dion, M.; Gingras, M. J. P.; Mason, T. E.; Greedan, J. E. *Phys. Rev. B* **1999**, *59*, 14489.
(10) Lee, J. S.; Moon, S. J.; Noh, T. W.; Takeda, T.; Kanno, R.; Yoshii, S.; Sato, M. *Phys. Rev. B* **2005**, *72*, 035124.
(11) Groult, D.; Pannetier, J.; Raveau, B. *J. Solid State Chem.* **1982**, *41*, 277.
(12) Ehlert, M. K.; Greedan, J. E.; Subramanian, M. A. *J. Solid State Chem.* **1988**, *75*, 188.
(13) Whittle, K. R.; Lumpkin, G. R.; Ashbrook, S. E. *J. Solid State Chem.* **2006**, *179*, 512.
(14) Uno, M.; Kosuga, A.; Okui, M.; Horisaka, K.; Muta, H.; Kurosaki, K.; Yamanaka, S. *J. Alloys Compd.* **2006**, *420*, 291.
(15) McCauley, R. A.; Hummel, F. A. *J. Lumin.* **1973**, *6*, 105.
(16) Zhang, A.; Lu, M.; Zhou, G.; Wang, S.; Zhou, Y. *J. Phys. Chem. Solids* **2006**, *67*, 2430.
(17) Yacobi, B. G., Holt, D. B. *Cathodoluminescence Microscopy of Inorganic Solids*; Plenum Press: New York, 1990.
(18) Tissue, B. M. *Chem. Mater.* **1998**, *10*, 2837.
(19) Lumpkin, G. R.; Whittle, K. R.; Rios, S.; Smith, K. L.; Zaluzec, N. J. *J. Phys.: Condens. Matter* **2004**, *16*, 8557.
(20) Subramanian, M. A.; Aravamudan, G.; Subba Rao, G. V. *Prog. Solid State Chem.* **1983**, *15*, 55.

(21) Panero, W. R.; Stixrude, L.; Ewing, R. C. *Phys. Rev. B* **2004**, *70*, 054110.
(22) Pirzada, M.; Grimes, R. W.; Minervini, L.; Maguire, J. F.; Sickafus, K. E. *Solid State Ionics* **2001**, *140*, 201.
(23) Wilde, P. J.; Catlow, C. R. A. *Solid State Ionics* **1998**, *112*, 173.
(24) Lian, J.; Chen, J.; Wang, L. M.; Ewing, R. C.; Farmer, J. M.; Boatner, L. A.; Helean, K. B. *Phys. Rev. B* **2003**, *68*, 134107.
(25) Glerup, M.; Nielsen, O. F.; Poulsen, F. W. *J. Solid State Chem.* **2001**, *160*, 25.
(26) Snyder, J.; Slusky, J. S.; Cava, R. J.; Schiffer, P. *Nature* **2001**, *413*, 48.
(27) Wilde, P. J.; Catlow, C. R. A. *Solid State Ionics* **1998**, *112*, 185.
(28) Díaz-Guillén, M. R.; Moreno, K. J.; Díaz-Guillén, J. A.; Fuentes, A. F.; García-Barriocanal, J.; Santamaría, J.; León, C. *Diffus. Defect Data, Part A* **2009**, *289*, 347.
(29) Riess, I.; Braunshtein, D.; Tannhauser, D. S. *J. Am. Ceram. Soc.* **1981**, *64*, 479.
(30) Zhang, L. L.; Zhang, W. G.; Zhu, J. W.; Lu, L. D.; Yang, X. J.; Wang, X. *J. Solid State Chem.* **2005**, *178*, 761.
(31) Zou, Z. G.; Ye, J. H.; Arakawa, H. *J. Phys. Chem. B* **2002**, *106*, 517.
(32) Uma, S.; Singh, J.; Thakral, V. *Inorg. Chem.* **2009**, *48*, 11624.
(33) Singh, J.; Uma, S. *J. Phys. Chem. C* **2009**, *113*, 12483.
(34) Uno, M.; Kosuga, A.; Okui, M.; Horisaka, K.; Muta, H.; Kurosaki, K.; Yamanaka, S. *J. Alloys Compd.* **2006**, *420*, 291.
(35) Pederson, L. R.; Chick, L. A.; Exarhos, G. J. U.S. Patent 5,114,702, May 19, 1992
(36) Jakkal, V. S. (BARC, Mumbai, India). *POWDERX: a FORTRAN software for refining the unit cell parameter for the powder diffraction pattern*, private communication.
(37) Rodríguez-Carvajal, J. *WinPLOTR*; Laboratorie Leon Brillouin (CEA-CNRS), April 2005 (LLB-LCSIM).
(38) Qu, Z.; Wan, C.; Pan, W. *Chem. Mater.* **2007**, *19*, 4913.
(39) Irvine, J. T. S.; Sinclair, D. C.; West, A. R. *Adv. Mater.* **1990**, *2*, 132.
(40) Shannon, R. D. *Acta Crystallogr.* **1976**, *A32*, 751.
(41) Vandenborre, M. T.; Husson, E.; Chatry, J. P.; Michel, D. *J. Raman Spectrosc.* **1983**, *14*, 63.
(42) Zhang, F. X.; Manoun, B.; Saxena, S. K.; Zha, C. S. *Appl. Phys. Lett.* **2005**, *86*, 181906.
(43) Scheetz, B. E.; White, W. B. *J. Am. Ceram. Soc.* **1979**, *62*, 468. Michel, D.; Perez, M. J.; Collongues, R. *Mater. Res. Bull.* **1974**, *9*, 1457.
(44) Mandal, B. P.; Dutta, A.; Deshpande, S. K.; Basu, R. N.; Tyagi, A. K. *J. Mater. Res.* **2009**, *24*, 2855.
(45) Keramidas, V. G.; White, W. B. *J. Chem. Phys.* **1973**, *59*, 1561.
(46) Tong, Y.; Yu, Z.; Lu, L.; Yang, X.; Wang, X. *Mater. Res. Bull.* **2008**, *43*, 2736.
(47) Qiang, X.; Wei, P.; Jingdong, W.; Longhao, Q.; Hezhuo, M.; Mori, K.; Torigoe, T. *Mater. Lett.* **2005**, *59*, 2804.
(48) Mandal, B. P.; Garg, N.; Sharma, S. M.; Tyagi, A. K. *J. Solid State Chem.* **2006**, *179*, 1990.
(49) Burggraaf, A. J.; van Dijk, T.; Verkerk, M. J. *Solid State Ionics* **1981**, *5*, 519.
(50) Yamamura, H.; Nishino, H.; Kakinuma, K.; Nomura, K. *Solid State Ionics* **2003**, *158*, 359.
(51) Andersen, O. K.; Jepsen, O. *Phys. Rev. Lett.* **1984**, *53*, 2571.
(52) Andersen, O. K.; Jepsen, O.; Glötzel, D. *Highlights of Condensed Matter Theory*; Bassani, F., Fumi, F., Tosi, M., Eds.; North-Holland: New York, 1985. Jepsen, O.; Andersen, O. K. *Z. Phys.:Condens Matter* **1995**, *97*, 35.
(53) Blöchl, P. E. *Phys. Rev. B* **1994**, *50*, 17953. Kresse, G.; Joubert, J. *Phys. Rev. B* **1999**, *59*, 1758.
(54) Lowdin, P. O. *J. Chem. Phys.* **1951**, *19*, 1396.
(55) Dong, S.; Song, S. *Electroanalysis* **1989**, *1*, 549.